

This work was written as part of one of the author's official duties as an Employee of the United States Government and is therefore a work of the United States Government. In accordance with 17 U.S.C. 105, no copyright protection is available for such works under U.S. Law.

Public Domain Mark 1.0

<https://creativecommons.org/publicdomain/mark/1.0/>

Access to this work was provided by the University of Maryland, Baltimore County (UMBC) ScholarWorks@UMBC digital repository on the Maryland Shared Open Access (MD-SOAR) platform.

**Please provide feedback**

Please support the ScholarWorks@UMBC repository by emailing [scholarworks-group@umbc.edu](mailto:scholarworks-group@umbc.edu) and telling us what having access to this work means to you and why it's important to you. Thank you.

# Hitomi X-ray studies of giant radio pulses from the Crab pulsar\*

Hitomi Collaboration, Felix AHARONIAN,<sup>1</sup> Hiroki AKAMATSU,<sup>2</sup>  
Fumie AKIMOTO,<sup>3</sup> Steven W. ALLEN,<sup>4,5,6</sup> Lorella ANGELINI,<sup>7</sup> Marc AUDARD,<sup>8</sup>  
Hisamitsu AWAKI,<sup>9</sup> Magnus AXELSSON,<sup>10</sup> Aya BAMBA,<sup>11,12</sup>  
Marshall W. BAUTZ,<sup>13</sup> Roger BLANDFORD,<sup>4,5,6</sup> Laura W. BRENNEMAN,<sup>14</sup>  
Gregory V. BROWN,<sup>15</sup> Esra BULBUL,<sup>13</sup> Edward M. CACKETT,<sup>16</sup>  
Maria CHERNYAKOVA,<sup>1</sup> Meng P. CHIAO,<sup>7</sup> Paolo S. COPPI,<sup>17,18</sup> Elisa COSTANTINI,<sup>2</sup>  
Jelle DE PLAA,<sup>2</sup> Cor P. DE VRIES,<sup>2</sup> Jan-Willem DEN HERDER,<sup>2</sup> Chris DONE,<sup>19</sup>  
Tadayasu DOTANI,<sup>20</sup> Ken EBISAWA,<sup>20</sup> Megan E. ECKART,<sup>7</sup> Teruaki ENOTO,<sup>21,22</sup>  
Yuichiro EZOE,<sup>23</sup> Andrew C. FABIAN,<sup>24</sup> Carlo FERRIGNO,<sup>8</sup> Adam R. FOSTER,<sup>14</sup>  
Ryuichi FUJIMOTO,<sup>25</sup> Yasushi FUKAZAWA,<sup>26</sup> Akihiro FURUZAWA,<sup>27</sup>  
Massimiliano GALEAZZI,<sup>28</sup> Luigi C. GALLO,<sup>29</sup> Poshak GANDHI,<sup>30</sup>  
Margherita GIUSTINI,<sup>2</sup> Andrea GOLDWURM,<sup>31,32</sup> Liyi GU,<sup>2</sup> Matteo GUAINAZZI,<sup>33</sup>  
Yoshito HABA,<sup>34</sup> Kouichi HAGINO,<sup>20</sup> Kenji HAMAGUCHI,<sup>7,35</sup> Ilana M. HARRUS,<sup>7,35</sup>  
Isamu HATSUKADE,<sup>36</sup> Katsuhiko HAYASHI,<sup>20</sup> Takayuki HAYASHI,<sup>37</sup>  
Kiyoshi HAYASHIDA,<sup>38</sup> Junko S. HIRAGA,<sup>39</sup> Ann HORNSCHMEIER,<sup>7</sup>  
Akio HOSHINO,<sup>40</sup> John P. HUGHES,<sup>41</sup> Yuto ICHINOHE,<sup>23</sup> Ryo IZUKA,<sup>20</sup>  
Hajime INOUE,<sup>42</sup> Yoshiyuki INOUE,<sup>20</sup> Manabu ISHIDA,<sup>20</sup> Kumi ISHIKAWA,<sup>20</sup>  
Yoshitaka ISHISAKI,<sup>23</sup> Masachika IWAI,<sup>20</sup> Jelle KAASTRA,<sup>2,43</sup> Tim KALLMAN,<sup>7</sup>  
Tsuneyoshi KAMAE,<sup>11</sup> Jun KATAOKA,<sup>44</sup> Satoru KATSUDA,<sup>45</sup> Nobuyuki KAWAI,<sup>46</sup>  
Richard L. KELLEY,<sup>7</sup> Caroline A. KILBOURNE,<sup>7</sup> Takao KITAGUCHI,<sup>26</sup>  
Shunji KITAMOTO,<sup>40</sup> Tetsu KITAYAMA,<sup>47</sup> Takayoshi KOHMURA,<sup>48</sup>  
Motohide KOKUBUN,<sup>20</sup> Katsuji KOYAMA,<sup>49</sup> Shu KOYAMA,<sup>20</sup>  
Peter KRETSCHMAR,<sup>50</sup> Hans A. KRIMM,<sup>51,52</sup> Aya KUBOTA,<sup>53</sup> Hideyo KUNIEDA,<sup>37</sup>  
Philippe LAURENT,<sup>31,32</sup> Shiu-Hang LEE,<sup>21</sup> Maurice A. LEUTENEGGER,<sup>7</sup>  
Olivier O. LIMOUSIN,<sup>32</sup> Michael LOEWENSTEIN,<sup>7</sup> Knox S. LONG,<sup>54</sup> David LUMB,<sup>33</sup>  
Greg MADEJSKI,<sup>4</sup> Yoshitomo MAEDA,<sup>20</sup> Daniel MAIER,<sup>31,32</sup> Kazuo MAKISHIMA,<sup>55</sup>  
Maxim MARKEVITCH,<sup>7</sup> Hironori MATSUMOTO,<sup>38</sup> Kyoko MATSUSHITA,<sup>56</sup>  
Dan McCAMMON,<sup>57</sup> Brian R. McNAMARA,<sup>58</sup> Missagh MEHDIPOUR,<sup>2</sup>  
Eric D. MILLER,<sup>13</sup> Jon M. MILLER,<sup>59</sup> Shin MINESHIGE,<sup>21</sup> Kazuhisa MITSUDA,<sup>20</sup>  
Ikuyuki MITSUISHI,<sup>37</sup> Takuya MIYAZAWA,<sup>60</sup> Tsunefumi MIZUNO,<sup>26</sup>  
Hideyuki MORI,<sup>7</sup> Koji MORI,<sup>36</sup> Koji MUKAI,<sup>7,35</sup> Hiroshi MURAKAMI,<sup>61</sup>  
Richard F. MUSHOTZKY,<sup>62</sup> Takao NAKAGAWA,<sup>20</sup> Hiroshi NAKAJIMA,<sup>38</sup>  
Takeshi NAKAMORI,<sup>63</sup> Shinya NAKASHIMA,<sup>55</sup> Kazuhiro NAKAZAWA,<sup>11</sup>  
Kumiko K. NOBUKAWA,<sup>64</sup> Masayoshi NOBUKAWA,<sup>65</sup> Hirofumi NODA,<sup>66,67</sup>  
Hirokazu ODAKA,<sup>6</sup> Takaya OHASHI,<sup>23</sup> Masanori OHNO,<sup>26</sup> Takashi OKAJIMA,<sup>7</sup>

Kenya OSHIMIZU,<sup>68</sup> Naomi OTA,<sup>64</sup> Masanobu OZAKI,<sup>20</sup> Frits PAERELS,<sup>69</sup>  
 Stéphane PALTANI,<sup>8</sup> Robert PETRE,<sup>7</sup> Ciro PINTO,<sup>24</sup> Frederick S. PORTER,<sup>7</sup>  
 Katja POTTSCHMIDT,<sup>7,35</sup> Christopher S. REYNOLDS,<sup>62</sup> Samar SAFI-HARB,<sup>70</sup>  
 Shinya SAITO,<sup>40</sup> Kazuhiro SAKAI,<sup>7</sup> Toru SASAKI,<sup>56</sup> Goro SATO,<sup>20</sup>  
 Kosuke SATO,<sup>56</sup> Rie SATO,<sup>20</sup> Makoto SAWADA,<sup>71</sup> Norbert SCHARTEL,<sup>50</sup>  
 Peter J. SERLEMTSOS,<sup>7</sup> Hiromi SETA,<sup>23</sup> Megumi SHIDATSU,<sup>55</sup>  
 Aurora SIMIONESCU,<sup>20</sup> Randall K. SMITH,<sup>14</sup> Yang SOONG,<sup>7</sup> Łukasz STAWARZ,<sup>72</sup>  
 Yasuharu SUGAWARA,<sup>20</sup> Satoshi SUGITA,<sup>46</sup> Andrew SZYMKOWIAK,<sup>17</sup>  
 Hiroyasu TAJIMA,<sup>3</sup> Hiromitsu TAKAHASHI,<sup>26</sup> Tadayuki TAKAHASHI,<sup>20</sup>  
 Shin'ichiro TAKEDA,<sup>60</sup> Yoh TAKEI,<sup>20</sup> Toru TAMAGAWA,<sup>55</sup> Takayuki TAMURA,<sup>20</sup>  
 Takaaki TANAKA,<sup>49</sup> Yasuo TANAKA,<sup>73</sup> Yasuyuki T. TANAKA,<sup>26</sup>  
 Makoto S. TASHIRO,<sup>68</sup> Yuzuru TAWARA,<sup>37</sup> Yukikatsu TERADA,<sup>68,†</sup>  
 Yuichi TERASHIMA,<sup>9</sup> Francesco TOMBESI,<sup>7,62</sup> Hiroshi TOMIDA,<sup>20</sup> Yohko TSUBOI,<sup>45</sup>  
 Masahiro TSUJIMOTO,<sup>20</sup> Hiroshi TSUNEMI,<sup>38</sup>  
 Takeshi Go TSURU,<sup>49</sup> Hiroyuki UCHIDA,<sup>49</sup> Hideki UCHIYAMA,<sup>74</sup>  
 Yasunobu UCHIYAMA,<sup>40</sup> Shutaro UEDA,<sup>20</sup> Yoshihiro UEDA,<sup>21</sup>  
 Shin'ichiro UNO,<sup>75</sup> C. Megan URRY,<sup>17</sup> Eugenio URSINO,<sup>28</sup> Shin WATANABE,<sup>20</sup>  
 Norbert WERNER,<sup>76,77,26</sup> Dan R. WILKINS,<sup>4</sup> Brian J. WILLIAMS,<sup>54</sup>  
 Shinya YAMADA,<sup>23</sup> Hiroya YAMAGUCHI,<sup>7</sup> Kazutaka YAMAOKA,<sup>3</sup>  
 Noriko Y. YAMASAKI,<sup>20</sup> Makoto YAMAUCHI,<sup>36</sup> Shigeo YAMAUCHI,<sup>64</sup>  
 Tahir YAQOOB,<sup>35</sup> Yoichi YATSU,<sup>46</sup> Daisuke YONETOKU,<sup>25</sup> Irina ZHURAVLEVA,<sup>4,5</sup>  
 Abderahmen ZOGHBI,<sup>59</sup> Toshio TERASAWA,<sup>55</sup> Mamoru SEKIDO,<sup>78</sup>  
 Kazuhiro TAKEFUJI,<sup>78</sup> Eiji KAWAI,<sup>78</sup> Hiroaki MISAWA,<sup>79</sup> Fuminori TSUCHIYA,<sup>79</sup>  
 Ryo YAMAZAKI,<sup>71</sup> Eiji KOBAYASHI,<sup>71</sup> Shota KISAKA,<sup>71</sup> and Takahiro AOKI<sup>80</sup>

<sup>1</sup>Dublin Institute for Advanced Studies, 31 Fitzwilliam Place, Dublin 2, Ireland

<sup>2</sup>SRON Netherlands Institute for Space Research, Sorbonnelaan 2, 3584 CA Utrecht, The Netherlands

<sup>3</sup>Institute for Space-Earth Environmental Research, Nagoya University, Furo-cho, Chikusa-ku, Nagoya, Aichi 464-8601, Japan

<sup>4</sup>Kavli Institute for Particle Astrophysics and Cosmology, Stanford University, 452 Lomita Mall, Stanford, CA 94305, USA

<sup>5</sup>Department of Physics, Stanford University, 382 Via Pueblo Mall, Stanford, CA 94305, USA

<sup>6</sup>SLAC National Accelerator Laboratory, 2575 Sand Hill Road, Menlo Park, CA 94025, USA

<sup>7</sup>NASA, Goddard Space Flight Center, 8800 Greenbelt Road, Greenbelt, MD 20771, USA

<sup>8</sup>Department of Astronomy, University of Geneva, ch. d'Écogia 16, CH-1290 Versoix, Switzerland

<sup>9</sup>Department of Physics, Ehime University, 2-5 Bunkyo-cho, Matsuyama, Ehime 790-8577

<sup>10</sup>Department of Physics and Oskar Klein Center, Stockholm University, 106 91 Stockholm, Sweden

<sup>11</sup>Department of Physics, The University of Tokyo, 7-3-1 Hongo, Bunkyo-ku, Tokyo 113-0033, Japan

<sup>12</sup>Research Center for the Early Universe, School of Science, The University of Tokyo, 7-3-1 Hongo, Bunkyo-ku, Tokyo 113-0033, Japan

<sup>13</sup>Kavli Institute for Astrophysics and Space Research, Massachusetts Institute of Technology, 77 Massachusetts Avenue, Cambridge, MA 02139, USA

<sup>14</sup>Harvard-Smithsonian Center for Astrophysics, 60 Garden Street, Cambridge, MA 02138, USA

<sup>15</sup>Lawrence Livermore National Laboratory, 7000 East Avenue, Livermore, CA 94550, USA

<sup>16</sup>Department of Physics and Astronomy, Wayne State University, 666 W. Hancock St, Detroit, MI 48201, USA

<sup>17</sup>Department of Physics, Yale University, New Haven, CT 06520-8120, USA

<sup>18</sup>Department of Astronomy, Yale University, New Haven, CT 06520-8101, USA

- <sup>19</sup>Centre for Extragalactic Astronomy, Department of Physics, University of Durham, South Road, Durham, DH1 3LE, UK
- <sup>20</sup>Japan Aerospace Exploration Agency, Institute of Space and Astronautical Science, 3-1-1 Yoshino-dai, Chuo-ku, Sagami-hara, Kanagawa 252-5210, Japan
- <sup>21</sup>Department of Astronomy, Kyoto University, Kitashirakawa-Oiwake-cho, Sakyo-ku, Kyoto, Kyoto 606-8502, Japan
- <sup>22</sup>The Hakubi Center for Advanced Research, Kyoto University, Yoshida-honmachi, Sakyo-ku, Kyoto, Kyoto 606-8501, Japan
- <sup>23</sup>Department of Physics, Tokyo Metropolitan University, 1-1 Minami-Osawa, Hachioji, Tokyo 192-0397, Japan
- <sup>24</sup>Institute of Astronomy, University of Cambridge, Madingley Road, Cambridge, CB3 0HA, UK
- <sup>25</sup>Faculty of Mathematics and Physics, Kanazawa University, Kakuma-machi, Kanazawa, Ishikawa 920-1192, Japan
- <sup>26</sup>School of Science, Hiroshima University, 1-3-1 Kagamiyama, Higashi-Hiroshima, Hiroshima 739-8526, Japan
- <sup>27</sup>Fujita Health University, 1-98 Dengakugakubo, Kutsukake-cho, Toyoake, Aichi 470-1192, Japan
- <sup>28</sup>Physics Department, University of Miami, 1320 Campo Sano Dr., Coral Gables, FL 33146, USA
- <sup>29</sup>Department of Astronomy and Physics, Saint Mary's University, 923 Robie Street, Halifax, NS, B3H 3C3, Canada
- <sup>30</sup>Department of Physics and Astronomy, University of Southampton, Highfield, Southampton, SO17 1BJ, UK
- <sup>31</sup>Laboratoire APC, 10 rue Alice Domon et Léonie Duquet, 75013 Paris, France
- <sup>32</sup>CEA Saclay, 91191 Gif sur Yvette, France
- <sup>33</sup>European Space Research and Technology Center, Keplerlaan 1 2201 AZ Noordwijk, The Netherlands
- <sup>34</sup>Department of Physics and Astronomy, Aichi University of Education, 1 Hirosawa, Igaya-cho, Kariya, Aichi 448-8543, Japan
- <sup>35</sup>Department of Physics, University of Maryland Baltimore County, 1000 Hilltop Circle, Baltimore, MD 21250, USA
- <sup>36</sup>Department of Applied Physics and Electronic Engineering, University of Miyazaki, 1-1 Gakuen Kibanadai-Nishi, Miyazaki, Miyazaki 889-2192, Japan
- <sup>37</sup>Department of Physics, Nagoya University, Furo-cho, Chikusa-ku, Nagoya, Aichi 464-8602, Japan
- <sup>38</sup>Department of Earth and Space Science, Osaka University, 1-1 Machikaneyama-cho, Toyonaka, Osaka 560-0043, Japan
- <sup>39</sup>Department of Physics, Kwansei Gakuin University, 2-1 Gakuen, Sanda, Hyogo 669-1337, Japan
- <sup>40</sup>Department of Physics, Rikkyo University, 3-34-1 Nishi-Ikebukuro, Toshima-ku, Tokyo 171-8501, Japan
- <sup>41</sup>Department of Physics and Astronomy, Rutgers University, 136 Frelinghuysen Road, Piscataway, NJ 08854, USA
- <sup>42</sup>Meisei University, 2-1-1 Hodokubo, Hino, Tokyo 191-8506, Japan
- <sup>43</sup>Leiden Observatory, Leiden University, PO Box 9513, 2300 RA Leiden, The Netherlands
- <sup>44</sup>Research Institute for Science and Engineering, Waseda University, 3-4-1 Ohkubo, Shinjuku-ku, Tokyo 169-8555, Japan
- <sup>45</sup>Department of Physics, Chuo University, 1-13-27 Kasuga, Bunkyo-ku, Tokyo 112-8551, Japan
- <sup>46</sup>Department of Physics, Tokyo Institute of Technology, 2-12-1 Ookayama, Meguro-ku, Tokyo 152-8550, Japan
- <sup>47</sup>Department of Physics, Toho University, 2-2-1 Miyama, Funabashi, Chiba 274-8510, Japan
- <sup>48</sup>Department of Physics, Tokyo University of Science, 2641 Yamazaki, Noda, Chiba 278-8510, Japan
- <sup>49</sup>Department of Physics, Kyoto University, Kitashirakawa-Oiwake-cho, Sakyo-ku, Kyoto, Kyoto 606-8502, Japan
- <sup>50</sup>European Space Astronomy Center, Camino Bajo del Castillo, s/n., 28692 Villanueva de la Cañada, Madrid, Spain
- <sup>51</sup>Universities Space Research Association, 7178 Columbia Gateway Drive, Columbia, MD 21046, USA

- <sup>52</sup>National Science Foundation, 4201 Wilson Blvd, Arlington, VA 22230, USA
- <sup>53</sup>Department of Electronic Information Systems, Shibaura Institute of Technology, 307 Fukasaku, Minuma-ku, Saitama, Saitama 337-8570, Japan
- <sup>54</sup>Space Telescope Science Institute, 3700 San Martin Drive, Baltimore, MD 21218, USA
- <sup>55</sup>Institute of Physical and Chemical Research, 2-1 Hirosawa, Wako, Saitama 351-0198, Japan
- <sup>56</sup>Department of Physics, Tokyo University of Science, 1-3 Kagurazaka, Shinjuku-ku, Tokyo 162-8601, Japan
- <sup>57</sup>Department of Physics, University of Wisconsin, Madison, WI 53706, USA
- <sup>58</sup>Department of Physics and Astronomy, University of Waterloo, 200 University Avenue West, Waterloo, Ontario, N2L 3G1, Canada
- <sup>59</sup>Department of Astronomy, University of Michigan, 1085 South University Avenue, Ann Arbor, MI 48109, USA
- <sup>60</sup>Okinawa Institute of Science and Technology Graduate University, 1919-1 Tancha, Onna-son, Kunigami-gun, Okinawa 904-0495, Japan
- <sup>61</sup>Faculty of Liberal Arts, Tohoku Gakuin University, 2-1-1 Tenjinzawa, Izumi-ku, Sendai, Miyagi 981-3193, Japan
- <sup>62</sup>Department of Astronomy, University of Maryland, College Park, MD 20742, USA
- <sup>63</sup>Faculty of Science, Yamagata University, 1-4-12 Kojirakawa-machi, Yamagata, Yamagata 990-8560, Japan
- <sup>64</sup>Department of Physics, Nara Women's University, Kitauoyanishi-machi, Nara, Nara 630-8506, Japan
- <sup>65</sup>Department of Teacher Training and School Education, Nara University of Education, Takabatake-cho, Nara, Nara 630-8528, Japan
- <sup>66</sup>Frontier Research Institute for Interdisciplinary Sciences, Tohoku University, 6-3 Aramaki-zaaoba, Aoba-ku, Sendai, Miyagi 980-8578, Japan
- <sup>67</sup>Astronomical Institute, Tohoku University, 6-3 Aramaki-zaaoba, Aoba-ku, Sendai, Miyagi 980-8578, Japan
- <sup>68</sup>Department of Physics, Saitama University, 255 Shimo-Okubo, Sakura-ku, Saitama, Saitama 338-8570, Japan
- <sup>69</sup>Astrophysics Laboratory, Columbia University, 550 West 120th Street, New York, NY 10027, USA
- <sup>70</sup>Department of Physics and Astronomy, University of Manitoba, Winnipeg, MB R3T 2N2, Canada
- <sup>71</sup>Department of Physics and Mathematics, Aoyama Gakuin University, 5-10-1 Fuchinobe, Chuo-ku, Sagami-hara, Kanagawa 252-5258, Japan
- <sup>72</sup>Astronomical Observatory of Jagiellonian University, ul. Orla 171, 30-244 Kraków, Poland
- <sup>73</sup>Max Planck Institute for Extraterrestrial Physics, Giessenbachstrasse 1, 85748 Garching, Germany
- <sup>74</sup>Faculty of Education, Shizuoka University, 836 Ohya, Suruga-ku, Shizuoka, Shizuoka 422-8529, Japan
- <sup>75</sup>Faculty of Health Sciences, Nihon Fukushi University, 26-2 Higashi Haemi-cho, Handa, Aichi 475-0012, Japan
- <sup>76</sup>MTA-Eötvös University Lendület Hot Universe Research Group, Pázmány Péter sétány 1/A, Budapest, 1117, Hungary
- <sup>77</sup>Department of Theoretical Physics and Astrophysics, Faculty of Science, Masaryk University, Kotlářská 2, Brno, 611 37, Czech Republic
- <sup>78</sup>Kashima Space Technology Center, National Institute of Information and Communications Technology, Kashima, Ibaraki 314-8501, Japan
- <sup>79</sup>Planetary Plasma and Atmospheric Research Center, Tohoku University, 6-3 Aoba, Aramaki, Aoba-ku, Sendai, Miyagi 980-8578, Japan
- <sup>80</sup>The Research Institute for Time Studies, Yamaguchi University, 1677-1 Yoshida, Yamaguchi 753-8511, Japan

\*Corresponding authors are Yukikatsu Terada, Teruaki Enoto, Shu Koyama, Aya Bamba, Toshio Terasawa, Shinya Nakashima, Tahir Yaqoob, Hiromitsu Takahashi, and Shin Watanabe.

†E-mail: [terada@phy.saitama-u.ac.jp](mailto:terada@phy.saitama-u.ac.jp)

Received 2017 July 21; Accepted 2017 July 27

## Abstract

To search for giant X-ray pulses correlated with the giant radio pulses (GRPs) from the Crab pulsar, we performed a simultaneous observation of the Crab pulsar with the X-ray satellite Hitomi in the 2–300 keV band and the Kashima NICT radio telescope in the 1.4–1.7 GHz band with a net exposure of about 2 ks on 2016 March 25, just before the loss of the Hitomi mission. The timing performance of the Hitomi instruments was confirmed to meet the timing requirement and about 1000 and 100 GRPs were simultaneously observed at the main pulse and inter-pulse phases, respectively, and we found no apparent correlation between the giant radio pulses and the X-ray emission in either the main pulse or inter-pulse phase. All variations are within the  $2\sigma$  fluctuations of the X-ray fluxes at the pulse peaks, and the  $3\sigma$  upper limits of variations of main pulse or inter-pulse GRPs are 22% or 80% of the peak flux in a 0.20 phase width, respectively, in the 2–300 keV band. The values for main pulse or inter-pulse GRPs become 25% or 110%, respectively, when the phase width is restricted to the 0.03 phase. Among the upper limits from the Hitomi satellite, those in the 4.5–10 keV and 70–300 keV bands are obtained for the first time, and those in other bands are consistent with previous reports. Numerically, the upper limits of the main pulse and inter-pulse GRPs in the 0.20 phase width are about  $(2.4 \text{ and } 9.3) \times 10^{-11} \text{ erg cm}^{-2}$ , respectively. No significant variability in pulse profiles implies that the GRPs originated from a local place within the magnetosphere. Although the number of photon-emitting particles should temporarily increase to account for the brightening of the radio emission, the results do not statistically rule out variations correlated with the GRPs, because the possible X-ray enhancement may appear due to a  $>0.02\%$  brightening of the pulse-peak flux under such conditions.

**Key words:** pulsars: individual (B0531+21) — radio continuum: stars — X-rays: stars

## 1 Introduction

Giant radio pulses (GRPs) consist of sporadic and short-lived radiation, during which time the radio flux density becomes 2–3 orders of magnitude brighter than the regular, averaged pulse flux density. So far, this phenomenon has been discovered in  $\sim 14$  radio pulsars (for a review, see Knight 2006 and references therein), including both “traditional” rotation-powered pulsars (e.g., the Crab pulsar) and millisecond pulsars (e.g., PSR B1937+21). Although the emission mechanism of the GRPs is still unknown, previous radio studies have shown some distinctive properties of the GRPs. The typical temporal width of individual GRPs is narrow, spanning a range from a few nanoseconds to a few microseconds (Hankins et al. 2003). GRPs occur in certain pulse phases with no clear periodicity. The energy spectrum of GRPs follows a power-law distribution (Popov & Stappers 2007; Majid et al. 2011; Mikami et al. 2016), different from the Gaussian or log-normal distributions of the normal pulses (Burke-Spolaor et al. 2012). Since studies of the ordinary pulses can only provide average information from the pulsar magnetosphere, observations of GRPs are imperative for furthering our understanding of the pulsar radiation mechanism. More recently, a hypothetical proposal of GRPs from young pulsars as

candidates for the origin of fast radio bursts (FRBs: Cordes & Wasserman 2016) has been attracting more and more attention. These phenomena are extragalactic bright radio transients with  $\sim 1$  ms duration (Lorimer et al. 2007; Thornton et al. 2013; Chatterjee et al. 2017). Seeking to reveal properties of known GRPs, such as identifying their counterparts in other wavelengths, is also a key line of investigation to examine the young pulsar model that could explain FRBs (e.g., Yamasaki et al. 2016; DeLaunay et al. 2016).

The Crab pulsar (PSR B0531+21) is one of the most intensively studied rotation-powered pulsars since the initial discovery of its GRPs (Staelin & Reifenstein 1968). This famous pulsar exhibits GRPs occurring in both the main pulse and the inter-pulse phases, which have been mainly studied at radio wavelengths (Popov & Stappers 2007). Since the pulsed energy spectrum of the Crab pulsar covers a wide range, from coherent radio emission to incoherent high-energy radiation of optical, X-rays, and gamma-rays, there have been multiwavelength campaigns to attempt to search for enhancements at higher energy bands, simultaneous with the GRPs. In the optical band, a significant 3% optical enhancement was discovered with  $7.2\sigma$  significance from the main



pulse peak phase by the Westerbork Synthesis Radio Telescope and the 4.2m William Herschel Telescope (Shearer et al. 2003). This result was further confirmed by the Green Bank Telescope and the Hale telescope (Strader et al. 2013). These detections imply that the coherent radio emission is somewhat linked to the incoherent higher-energy (optical) radiation. Despite intensive efforts to search at even higher energy bands, so far there are only upper limits in soft X-rays and higher energy bands. Reports of these upper limits can be found for soft X-rays (Chandra, 1.5–4.5 keV: Bilous et al. 2012), for soft gamma-rays (CGRO/OSSE, 50–220 keV: Lundgren et al. 1995), for gamma-rays (Fermi/LAT, 0.1–5 GeV: Bilous et al. 2011), and for very high-energy gamma-rays (VERITAS, >150 GeV: Aliu et al. 2012).

The X-ray astronomical satellite Hitomi (ASTRO-H) was launched on 2016 February 17 via an H-IIA launch vehicle from Tanegashima Space Center in Japan, and successfully entered into a low Earth orbit at an altitude of 575 km (Takahashi et al. 2018). The satellite was designed to cover a wide energy range from 0.3 keV to 600 keV with four new X-ray instruments: the microcalorimeter (Soft X-ray Spectrometer, SXS: Kelley et al. 2018), a wide field-of-view X-ray CCD detector (Soft X-ray Imager, SXI: Tanaka et al. 2018, Nakajima et al. 2018), two Si/CdTe hybrid hard X-ray imagers (Hard X-ray Imager, HXI: Nakazawa et al. 2018), and a Compton telescope (Soft Gamma-ray Detector, SGD: Tajima et al. 2018). Such a wide energy coverage with high time resolution at a few microseconds (Terada et al. 2017) made Hitomi suitable for the search for X-ray enhancement simultaneously with the GRPs. After initial operations before opening the gate valve of the SXS, including successful observations of the Perseus cluster of galaxies (Hitomi Collaboration 2016) and other supernova remnants (e.g., N132 D and G21.5–0.9), the spacecraft lost communications with the ground stations on March 26, and eventually the mission was terminated. Therefore, the energy coverage below 2 keV was lost for the SXS.

On March 25, just before the satellite loss, we observed the Crab pulsar with Hitomi for onboard instrumental calibration activity. The requirement and goal of the absolute timing accuracy of the Hitomi satellite are 350  $\mu$ s and 35  $\mu$ s, respectively (Terada et al. 2017). In order to verify the timing tag accuracy, we compared arrival times of the main pulse peak of the Crab pulsar with the radio or X-ray ephemeris provided by other observatories (Terada et al. 2008). The archival monthly radio ephemeris of the Crab pulsar has been regularly provided by the Jodrell Bank observatory<sup>1</sup> on every 15th monitoring (Lyne et al. 1993).

**Table 1.** Crab ephemeris in radio.\*

Parameter	Value
Main pulse	MJD 57472.0000002874260532
Period	0.0337204396077250 s
Period derivative	$4.1981605 \times 10^{-13} \text{ s s}^{-1}$

\*Ephemeris of the Crab pulsar determined by the radio observations on 2016 March 25. “Main pulse” represents the arrival time of the main pulse in the radio band. All values are in TDB.

Interpolating from this, the predicted ephemeris of the Crab pulsar timing in barycentric dynamical time (TDB) is tabulated in table 1.

The arrival times of the radio pulses are known to be delayed relative to that of X-rays in proportion to the interstellar dispersion measure (DM). The long-term, averaged DM of the Crab pulsar is  $\sim 56.8 \text{ pc cm}^{-3}$ , corresponding to  $\sim 120 \text{ ms}$  delay of the 1.4 GHz radio pulses relative to X-rays. Although this radio delay is corrected via radio analyses (dedispersion), this DM is known to show fluctuation in time with  $\sim 0.028 \text{ pc cm}^{-3}$  ( $1\sigma$ ) of a Gaussian distribution. This corresponds to an intrinsic uncertainty of  $\sim 60 \mu$ s timing accuracy, which prevents us from achieving the goal for the timing accuracy (35  $\mu$ s). Therefore, we coordinated follow-up radio observations simultaneous with our X-ray observations to reduce uncertainties due to this fluctuating DM. In this paper, we report on X-ray studies of GRPs from the Crab pulsar based on simultaneous X-ray and radio observations. Detailed investigations of the instrumental timing calibration will be summarized in a different paper (K. Koyama et al. in preparation).

## 2 Observations and data reduction

### 2.1 Simultaneous observation of X-ray and radio of the Crab pulsar

The X-ray observation of the Crab pulsar was made with all the instruments on board the Hitomi satellite, starting at 12:17 on 2016 March 25 until 18:01 UT [TDB], with a total on-source duration of 9.7 ks. The radio observations of the Crab pulsar were made in two bands of frequencies, (a) 1.4–1.7 GHz at the Kashima observatory from 03:00:00 to 14:00:00 UTC, and (b) 323.1–327.1 MHz at the Iitate observatory from 09:30:00 to 13:00:00 UTC. The locations of the observatories are listed in table 1 of Mikami et al. (2016). After the starting time of the X-ray observation we identified 3350 GRPs (sub-subsection 2.2.4) for (a), but only 94 GRPs for (b). In terms of the occurrence probability (number of GRPs per minute), the ratio between (a) and (b) was  $\sim 19:1$ . Mikami et al. (2016) reported, on the other hand, that the ratio was  $\sim 3:1$  on 2014 September 6–7. The marked difference between these ratios seems to be caused

<sup>1</sup> (<http://www.jb.man.ac.uk/pulsar/crab/crab2.txt>).

**Table 2.** Frequency bands of the Kashima observatory.\*

Channel $k$	Frequency (MHz) minimum–maximum	Original bandwidth (MHz)	Effective bandwidth (MHz) after filtering ( $\Delta\nu_k$ )
ch0	1404–1436	32	20.48
ch1	1570–1602	32	16.00
ch2	1596–1628	32	—
ch3	1622–1654	32	—
ch4	1648–1680	32	24.83
ch5	1674–1706	32	21.82
ch6	1700–1732	32	23.23
(ch7)	(1702–1734)	(32)	—

\*The frequency range between ch0 and ch1, 1436–1570 MHz, is avoided so as to minimize the radio frequency interference (RFI) from cellphone base stations. Only the right-hand circular polarized signals were received. In the coherent dedispersion process for each channel, the timing of the voltage data is adjusted to that for the maximum frequency of the channel.

by refractive interstellar scintillation (RISS; e.g., Lundgren et al. 1995): While the RISS condition for 1.4–1.7 GHz would have corresponded to a phase of the intensity larger than the average, the RISS condition for 325 MHz would have corresponded to a phase of the intensity smaller than the average. Therefore we concentrate on observation (a) in what follows.

## 2.2 Data reduction of radio observations

### 2.2.1 Frequency assignment

The radio observation in the 1.4–1.7 GHz band was made with the 34 m telescope at the Kashima Space Technology Center (Takefujii et al. 2016) operated by the NICT (National Institute of Information and Communications Technology). We used the ADS3000+ recorder (Takefujii et al. 2010), which has a capability of eight individual channels with four-bit 64 MHz Nyquist-rate sampling. (The sampling time step  $\delta t$  is  $1/64$  MHz = 15.625 ns, and the data rate is 2 Gbits s<sup>-1</sup>.) Table 2 shows the frequency assignments for the eight channels. Channel 7, the backup for channel 6 with a slight frequency shift, was not used for the following data analysis.

### 2.2.2 Determination of DM

We first determined the DM appropriate for the epoch of the observation, 2016 March 25 (MJD 57472). While the Jodrell Bank Crab pulsar monthly ephemeris reports the values of  $56.7657$  pc cm<sup>-3</sup> ( $= DM_{JB}$ ) for 2016 March 15 (MJD 57462), and  $56.7685$  pc cm<sup>-3</sup> for 2016 April 15 (MJD 57493), we should take into account possible intra-month variations of DM which are sometimes very erratic (e.g., Kuzmin et al. 2008). With  $DM_{JB}$  as a trial value, we coherently dedispersed (Hankins & Rickett 1975; Lorimer & Kramer 2004) the ch0 data and found several bright GRPs. We then extended the dedispersion analysis to all the channels for  $\sim 50$  ms intervals including these GRPs. The

best value of DM,  $56.7731 \pm 0.0001$  pc cm<sup>-3</sup> ( $= DM_{best}$ ), was obtained so as to get the alignment of the substructures of these GRPs (e.g., Sallmen et al. 1999) in all channels with  $\sim 0.1$   $\mu$ s accuracy. An example of a successful alignment can be seen in figure 2 of Mikami et al. (2016). Their bands of frequencies, LL and LH, approximately correspond to ch1 and ch4–ch6 here, respectively.

### 2.2.3 Frequency-domain RFI rejection

During the process of finding  $DM_{best}$ , we noticed that two channels, ch2 and ch3, were severely contaminated by radio frequency interface (RFI). Since the RFI occurred intermittently, we could still use these channels for the bright GRP search. However, for weaker GRPs, we excluded ch2 and ch3 from the following analysis. We further noticed that other channels were weakly contaminated by RFI in some limited frequency ranges. To minimize the effect of RFI, we filtered out these contaminated ranges of frequencies. The numerical filter was applied at the first stage of the coherent dedispersion process, where a time series of antenna voltage data is subjected to FFT (fast Fourier transformation) and decomposed into Fourier components. For the RFI-contaminated frequency ranges, we set their Fourier components to zero. The overlapping frequency ranges for ch4–ch5 and ch5–ch6 are also filtered out at this stage. The rightmost column of table 2 gives the resultant effective bandwidths after filtering. The total effective bandwidth,  $\Delta\nu_{sum} = \Delta\nu_0 + \Delta\nu_1 + \dots + \Delta\nu_6$ , is 106.36 MHz.

### 2.2.4 GRP selection

In the main panel of figure 1, dots show all GRP candidates with a  $S/N$  (signal-to-noise ratio)  $> 5.5$  (or pulse energy  $\gtrsim 2.2$  kJy  $\mu$ s, see appendix 1), where the dots are sized and color-coded with the values of  $S/N$ . The abscissa and ordinate of the panel represent the time in TDB and the pulsar rotation phase  $\varphi$  respectively. The top panel of figure 1



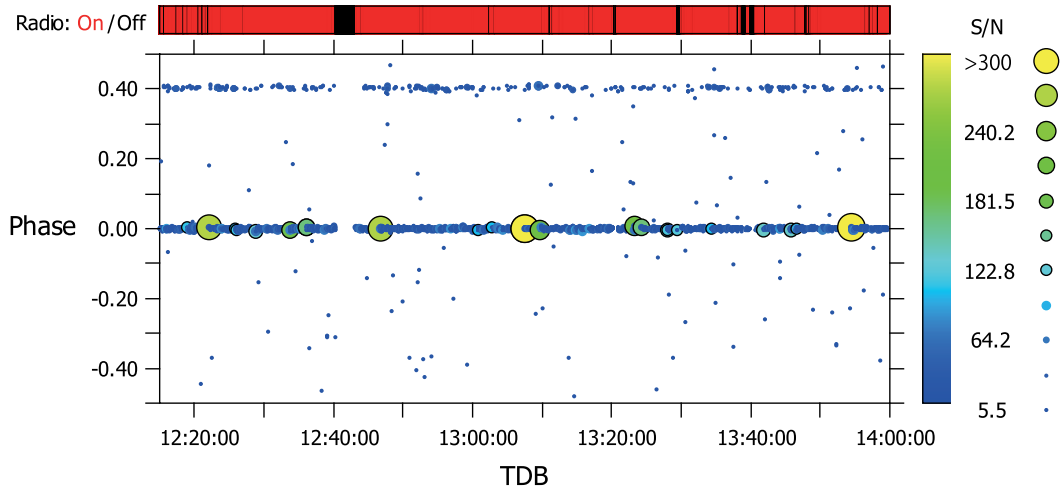


**Fig. 1.** In the main panel, GRP candidates ( $S/N > 5.5$ ) are shown in the (TDB,  $\varphi$ ) plane, where two clusters in  $\varphi$  are of main pulse and inter-pulse GRPs (see text). Scattered points show the remaining noise contribution. The threshold  $S/N = 5.5$  corresponds to the minimum pulse energy  $2.2 \text{ kJy } \mu\text{s}$ . The strongest main pulse occurred at 2016 March 25 13:07:25.645 TDB and had a peak  $S/N \sim 659$ . It extended over an  $\sim 40 \mu\text{s}$  interval, having a total pulse energy of  $358 \text{ kJy } \mu\text{s}$ . (Color online)

shows the time intervals subjected to the time-domain RFI rejection (see appendix 1) in black (OFF), and the time intervals kept, in red (ON). In total, 571 s (5729 s) in time intervals were rejected (kept).

As can be seen in figure 1, there are two clusters of GRP candidates in  $\varphi$ . We adjusted the initial value of  $\varphi$  at 00:00:00 TDB [ $y_0$  in equation (A6)] so as to locate the peak of the main cluster at  $\varphi = 0$ , which is the main pulse GRPs (hereafter we call them the “MP-GRP”). The second cluster, found around  $\varphi = 0.4056$ , corresponds to the inter-pulse GRPs (hereafter “IP-GRP”). The scattered points also seen in figure 1 are due to the noise component. With the selection criteria (1)  $-0.0167 \leq \varphi \leq +0.0167$  for the MP-GRPs and (2)  $0.3889 \leq \varphi \leq 0.4222$  for the IP-GRPs, we identified 3090 MP-GRPs and 260 IP-GRPs during the interval between 12:15:00 TDB and 14:00:00 TDB. We estimated the noise contributions in terms of fake GRPs to be  $11\% \pm 3$  ( $0.4\% \pm 0.1\%$  for the MP-GRPs and  $4\% \pm 1\%$  for the IP-GRPs). The pulse energy distributions of GRPs have power-law shapes with spectral indices  $-2.88 \pm 0.52$  for the MP-GRPs and  $-2.91 \pm 1.13$  for the IP-GRPs.

### 2.3 Data reduction of Hitomi observations

The X-ray data obtained with the Hitomi satellite were processed by the standard Hitomi pipeline version 03.01.005.005 (Angelini et al. 2017) with the pre-pipeline version 003.012.004p2.004 using the Hitomi ftools in HEASoft version 6.20, with CALDB versions gen20161122, hxi20161122, sgd20160614, sxi20161122, and sxs20161122. In the timing analyses of Hitomi data

in the following sections, the SXS and SGD-2 data were not used, because the timing resolution of the SXS was insufficient for the analyses and the SGD-2 was not in the nominal operation mode during the epoch simultaneous with the radio observation.

The standard cleaned events were used for the SXS and HXI analyses: the low-resolution events (ITYPE = 3 or 4; Kelley et al. 2018) of the SXS events were not excluded in order to maximize the statistics, although the time resolution of the low-resolution events ( $80 \mu\text{s}$ ) was worse than those of high- or medium-resolution events ( $5 \mu\text{s}$ ). The HXI data were extracted to use a sky image region around the Crab pulsar, within a radius of  $70''$  from the image centroid. On the analyses of the SGD-1 data, the photo-absorption events were extracted as described in appendix 2. At this stage, the total exposure times of the Hitomi Crab observation were 9.7, 8.0, and 8.6 ks for the SXS, HXI, and SGD-1, respectively. The background-inclusive light curves of these data are shown in black in figure 2. Note that no energy selection was applied to the events: the rough energy bands for the SXS, HXI, and SGD-1 photo-absorption events were 2–10 keV, 2–80 keV, and 10–300 keV, respectively.

The TIME columns of all the event lists of SXS, HXI, and SGD-1 were converted into a barycentric position using the *barycor* ftool in the Hitomi package of HEASoft 6.20 and the Hitomi orbital file (Terada et al. 2017). The target position for the barycentric correction was (RA, Dec)<sub>J2000.0</sub> = (83°633218, +22°014464) for these analyses. The period and its derivative determined only with the Hitomi data were consistent with the ephemeris from the radio summarized in table 1. As described in Terada et al. (2017) and K. Koyama et al. (in preparation), the time differences

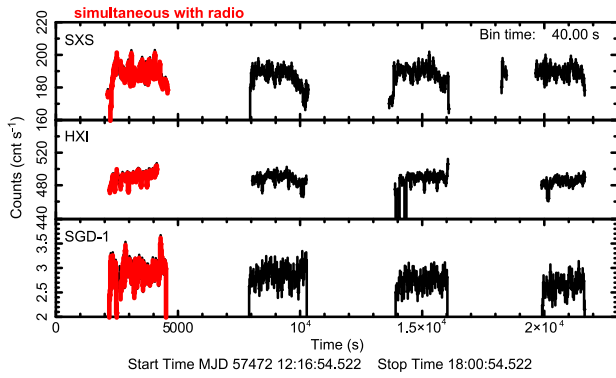


**Fig. 2.** Light curve of the Crab pulsar from Hitomi SXS (top), HXI, and SGD-1 (bottom). The black curves represent the entire cleaned events of the Crab pulsar with Hitomi, and red ones show the same but within the period under the simultaneous observation of Hitomi and the radio observatories. (Color online)

**Table 3.** Statistics of GRPs during the simultaneous observation.\*

Instrument	Exposure	# of cycles	MP-GRPs	IP-GRPs
SXS	2.2 ks	64701	1171	103
HXI	1.7 ks	50705	945	85
SGD	2.1 ks	63197	1144	98

\*Total exposures, number of cycles of pulsar pulses, and number of GRPs for main pulse and inter-pulse, during the simultaneous observation of radio observatories and Hitomi instruments.

between instruments were negligible for the timing analyses of the GRPs reported here.

Finally, all the good time intervals of the radio observation were applied to the Hitomi Crab data, which then results in a shorter duration, as shown in figure 2 (red). Consequently, the total exposure times for the SXS, HXI, and SGD-1 that were simultaneously observed with the radio observatories become 2.7, 1.7, and 2.1 ks, respectively. About  $10^3$  GRP cycles were exposed among  $(5-6) \times 10^4$  cycles by each instrument, as summarized in table 3.

### 3 Analyses and results

In this section, we used the cleaned events obtained with the Hitomi SXS/HXI/SGD instruments at the end of the subsection 2.3 and the pulsar ephemeris in table 1.

#### 3.1 Variation of the pulse profiles in GRPs

Most significant MP- and IP-GRPs, shown as large circles in figure 1, were detected at 12:46:44 and 12:54:10 (TDB) on 2016 May 25, respectively, but no significant variations were seen in the X-ray photons before or after the GRPs. Therefore, we then tried to stack X-ray events that were correlated with MP- or IP-GRPs to see a possible

enhancement in the X-ray band. X-ray events within one cycle of each MP-GRP (hereafter we call them the “MP-GRP cycles”) were accumulated between the  $\varphi = -0.5$  to  $+0.5$  phases from the arrival time of the main pulse of the radio-defined MP-GRPs (i.e.,  $\varphi = 0$ ). The events outside the MP-GRP cycles were defined as “NORMAL cycles” and were accumulated for comparison. Both groups of events were folded by the radio ephemeris in table 1 to see the pulse profiles of MP-GRP and NORMAL cycles. As shown in the top panels of the left-hand plots in figure 3, no major enhancements could be seen between the two profiles. The difference between the two, shown in the bottom panels, was consistent with being statistically constant among all the instruments and along all of the phases ( $-0.5 \leq \varphi \leq 0.5$ ). Note that the pulse profile of the Crab pulsar with the SXS is free from possible distortion by the dead time, which occurs in  $>5$  s on the SXS. Similarly, the distortion of the profiles of the HXI and SGD-1 can be also ignored in comparison between the GRP and NORMAL shapes, although the absolute fractions of the dead to the live times were about 75% (subsection 3.3). The same analyses were performed for the inter-pulse GRPs (hereafter, “IP-GRP cycles”), and no significant enhancement between pulse profiles at IP-GRP and another NORMAL cycles was found, as seen in figure 3 (right). The statistical errors were very high on the Hitomi datasets, in both MP- and IP-GRPs.

In order to see some possible enhancements in several cycles around the GRPs in a wider time range, we then accumulated the events from two cycles before the MP-GRPs to two cycles after; i.e., five pulses  $-2.5 < \varphi < 2.5$  were plotted where  $-0.5 \leq \varphi \leq 0.5$  corresponds to the MP-GRP cycle. Similarly in the case of the previous single-pulse analyses, the NORMAL cycles here were defined outside the five cycles around the MP-GRPs. The results are shown in figure 4. According to the time intervals between GRPs, about 0.7% and 2.4% of MP-GRPs were contaminated within  $\pm 1$  or  $\pm 2$  cycles of the GRP, respectively. To estimate the statistical errors on the pure-pulsed components, the non-pulsed counts accumulated from the OFF phase ( $\varphi = 0.6-0.8$ ) were subtracted from the pulse profiles of the MP-GRP and NORMAL cycles. Several possible enhancements can be seen in several main pulses in the soft energy band by the SXS in the top panels of figure 4; however, the significance was all below  $2\sigma$ , as indicated in the bottom panels, and no corresponding enhancement was seen in the hard X-ray band by the HXI. The same study was performed for IP-GRPs but the statistical errors were very high and the results were the same as for the MP-GRP cases. Therefore, no enhancements were detected in all phases among five cycles around GRPs from the Hitomi data.

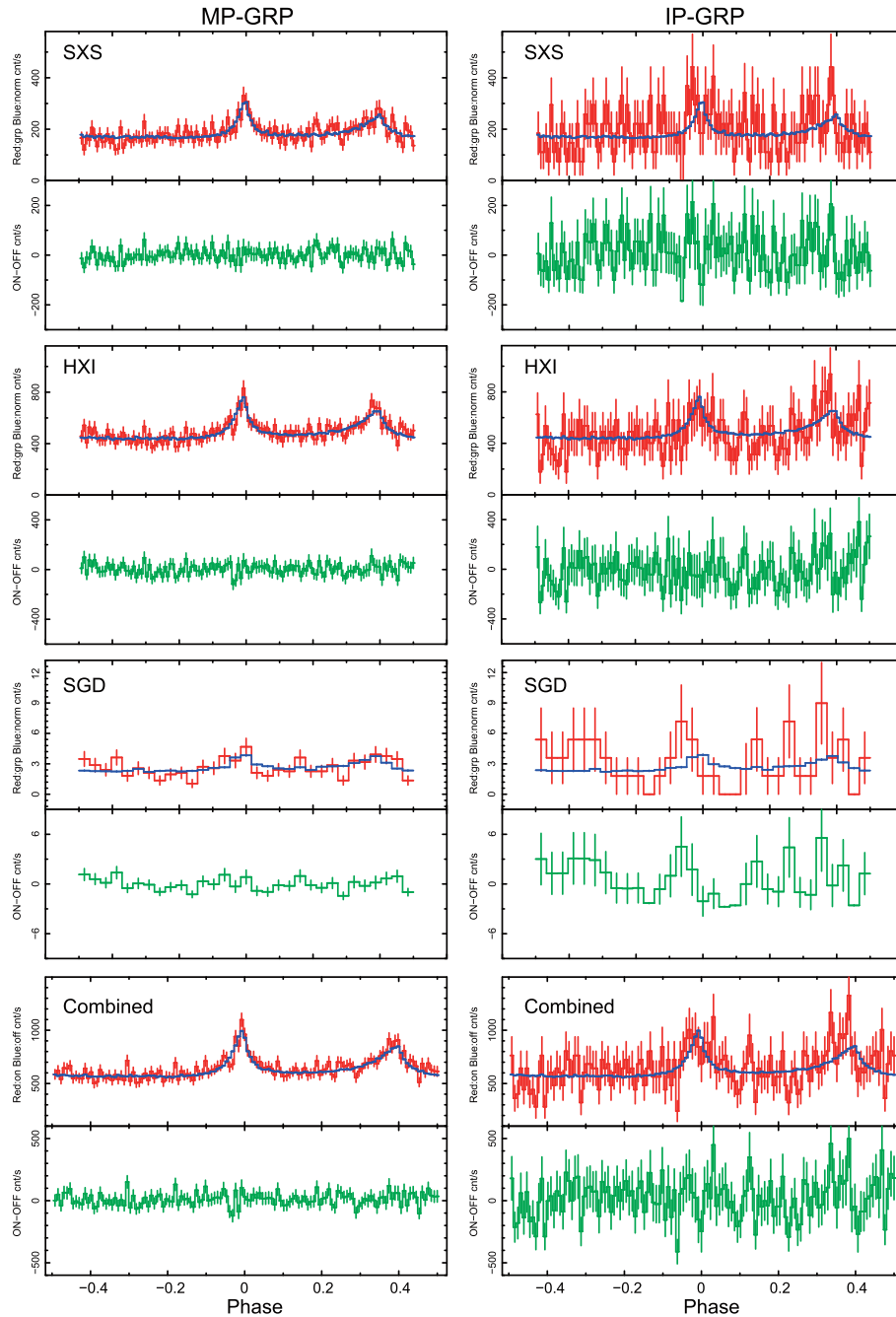


**Fig. 3.** Comparison of Crab pulse profiles between the NORMAL and the GRP cycles, shown in blue and red, respectively, and the green crosses in the lower panels show the difference between them. The left- and right-hand panels are plots of the MP-GRPs and IP-GRPs, respectively, and from the top to the bottom, the data taken by the SXS, HXI, SGD-1, and combined data, respectively. (Color online)

### 3.2 Pulse peak enhancement at GRPs

Since no significant enhancement was found in five cycles before/after GRPs (subsection 3.1), we then concentrated on the statistical tests of possible enhancements at the peaks of the pulses. Here, we compared the non-pulse subtracted peak-counts ( $C_{\text{grp}}$ ) of main pulses or inter-pulses of MP-GRP or IP-GRPs with those of corresponding NORMAL cycles ( $C_{\text{nor}}$ ). In this comparison, we defined

four types of phase widths ( $\Delta\varphi$ ) to accumulate the peak counts:  $\Delta\varphi = 0.20$  phases (covering main pulses or inter-pulses),  $1/11$ ,  $1/31$ , and  $1/128$  phases. The enhancement of  $C_{\text{grp}}$  from  $C_{\text{nor}}$  accumulated within  $\Delta\varphi$  can be defined as  $\xi(\Delta\varphi) \equiv [C_{\text{grp}}(\Delta\varphi) - C_{\text{nor}}(\Delta\varphi)]/[C_{\text{nor}}(\Delta\varphi)]$ . Table 4 summarizes  $\xi(\Delta\varphi)$  for each  $\Delta\varphi$ , shown as a percentage, for each instrument, with the significance to the statistical errors. As a result, no larger than a  $2\sigma$  enhancement was detected

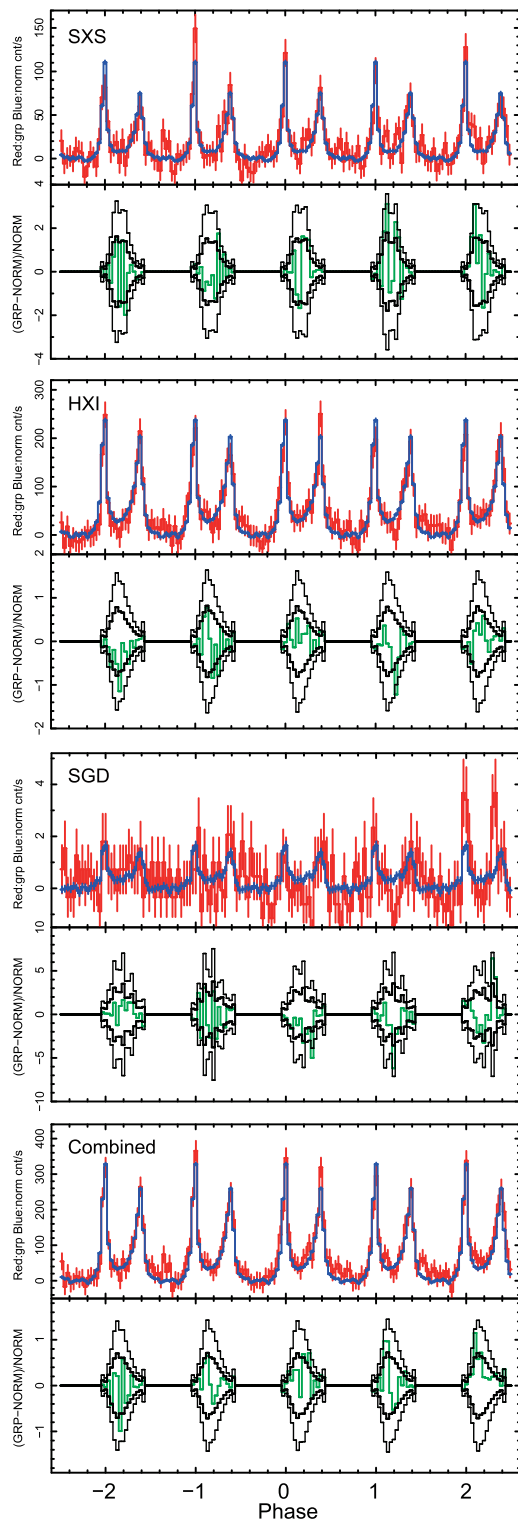


**Fig. 4.** The upper plots in each panel show the same pulse profiles of NORMAL and on/near GRP cycles represented by blue and red lines, respectively. The counts in the off-phase ( $\varphi = 0.6\text{--}0.8$ ) of the NORMAL cycles were subtracted from these pulse profiles. The lower plots in each panel represent the ratio of the enhancement of near GRP data relative to the NORMAL cycles, which are shown in green. The data during the OFF phase are not plotted here. The statistical uncertainties of each phase bin at  $1\sigma$  and  $2\sigma$  are shown in thick black and thin black lines, respectively. The SXS, HXI, SGD-1, and combined data are shown in the panels from top to bottom. (Color online)

around GRPs in all cases. The fluctuation got smaller when we restricted the phase width for MP-GRPs due to the sharp pulse profile of the main pulse, except for the  $\Delta\varphi = 1/128$  ( $\sim 0.008$ ) phase-width cases with poorer photon statistics, although such a trend could not be seen for the inter-pulses that had a shallower shape.

To test the enhancement  $\xi(\Delta\varphi)$  at the snapshot on GRP ( $\varphi = 0$ ), same trials were repeated for 29 cycles around the GRP, i.e., the 14 cycles before to the 14 cycles after the MP-GRP or IP-GRP ( $-14.5 \leq \varphi \leq 14.5$ ), as plotted in figure 5. Therefore, a possible enhancement at  $\varphi = 0$  was within the fluctuations of  $\xi(\Delta\varphi)$  in other cycles to within  $2\sigma$  variations for  $28 + 1$  cycles. Numerically, the  $3\sigma$  upper limits of the variations at the MP-GRP during the main pulse phases (i.e.,  $\varphi = -0.1\text{--}0.1$ , with 0.200 phase width in figure 5) will be  $\xi_{\text{MPGRP}}(0.200 \text{ phase}) = 40\%$ ,  $30\%$ , and  $110\%$  of the X-ray flux in the NORMAL cycles, with the SXS, HXI, and SGD-1 corresponding roughly to the 2–10, 2–80, and 10–300 keV bands. Similarly, the  $3\sigma$  upper limits for the IP-GRP during inter-pulse phases ( $\varphi = 0.3\text{--}0.5$ ) were  $\xi_{\text{IPGRP}}(0.200 \text{ phase}) = 130\%$ ,  $90\%$ , and  $420\%$  in the same energy bands listed above, respectively. When all of the instruments (i.e., the SXS, HXI, and SGD-1) were used for this study, the upper-limit values become tighter at  $\xi(0.200 \text{ phase}) = 22\%$  and  $80\%$  of the NORMAL cycles for the MP- and IP-GRPs, respectively. In addition, in order to see a possible enhancement on a short-time scale around the peaks of pulses, as seen in the optical observations (Shearer et al. 2003; Strader et al. 2013), the enhancements of MP- and IP-GRPs accumulated within the  $\Delta\varphi = 1/31$  ( $\sim 0.03$ ) phase width were also numerically checked:  $\xi(0.03 \text{ phase}) = 25\%$  and  $110\%$  for MP- and IP-GRPs were obtained. The  $3\sigma$  upper limits of  $\xi$  from the 29 cycles study are summarized in table 5.

### 3.3 Upper limit of enhanced peak flux

To convert the enhancement of GRP in count rate into an X-ray flux, the X-ray spectra of purely pulsed components (i.e., main pulse and inter-pulse) were numerically tested. First, the SXS and HXI events were extracted by phases— $\varphi = -0.1\text{--}0.1$ ,  $\varphi = 0.3\text{--}0.5$ , and  $\varphi = 0.6\text{--}0.8$ , corresponding to the main-pulse (MP), inter-pulse (IP), and off (OFF) phases, respectively—and the pulse height distributions were accumulated. The dead time correction was applied to the HXI data with the Hitomi tool *hxisgddtime*; the live time of the HXI-1 and HXI-2 were 73.9% and 76.6% for this observation. Only the high-primary and the medium-primary grades (Hp and Mp grades, respectively, as defined in Kelley et al. 2018) were accumulated in the SXS spectral analyses here in order to reduce systematic errors in the response matrix. The X-ray spectra of the

**Table 4.** Summary of enhancements in X-ray flux at GRPs.\*

Instrument	Pulse	0.0078 phase <sup>†</sup>	0.0322 phase <sup>†</sup>	0.091 phase <sup>†</sup>	0.200 phase <sup>†</sup>
SXS	main pulse	1% (0.0 $\sigma$ )	10% (0.7 $\sigma$ )	1% (0.1 $\sigma$ )	7% (0.6 $\sigma$ )
SXS	inter-pulse	310% (1.6 $\sigma$ )	93% (1.3 $\sigma$ )	55% (1.1 $\sigma$ )	31% (0.6 $\sigma$ )
HXI	main pulse	11% (0.5 $\sigma$ )	−2% (−0.2 $\sigma$ )	−5% (−0.6 $\sigma$ )	6% (0.7 $\sigma$ )
HXI	inter-pulse	136% (1.4 $\sigma$ )	78% (1.3 $\sigma$ )	29% (0.9 $\sigma$ )	49% (1.5 $\sigma$ )
SGD-1	main pulse	−116% (1.2 $\sigma$ )	−39% (0.7 $\sigma$ )	−43% (−1.0 $\sigma$ )	−59% (−1.4 $\sigma$ )
SGD-1	inter-pulse	310% (1.6 $\sigma$ )	93% (1.3 $\sigma$ )	55% (1.1 $\sigma$ )	31% (0.6 $\sigma$ )
Combined	main pulse	8.9% (0.5 $\sigma$ )	5.1% (0.6 $\sigma$ )	−0.8% (−0.1 $\sigma$ )	13.2% (1.8 $\sigma$ )
Combined	inter-pulse	195% (2.2 $\sigma$ )	45% (1.2 $\sigma$ )	50% (1.8 $\sigma$ )	66.5% (2.4 $\sigma$ )

\*The values represent the enhancement  $\xi(\Delta\phi)$  (%), and values in parentheses show the significance in the standard deviation of each to the statistical errors.

<sup>†</sup>The phase width ( $\Delta\phi$ ).

pure-pulsed components were calculated by subtraction of the OFF-phase spectrum from the MP or IP spectra. Thanks to the fine timing resolutions of the SXS, HXI, and SGD-1 (Terada et al. 2017), the X-ray spectra of the pure-pulsed components are clearly demonstrated in figure 6.

To perform spectral fitting of the MP and IP spectra, the spectral response matrices were generated with the Hitomi tools *sxsmkrmf* and *aharfgen*, with the exposure map calculated for HXI and SXS using the tools *sxs-regext* and *ahexpmap*, respectively. The result was that the MP and IP spectra were well reproduced by a single power-law model with photon indices of  $1.94 \pm 0.02$  and  $1.87 \pm 0.02$  and X-ray fluxes of  $(4.7 \pm 0.1) \times 10^{-9}$  and  $(4.4 \pm 0.5) \times 10^{-9} \text{ erg cm}^{-2} \text{ s}^{-1}$  in the 2–10 keV band with the reduced  $\chi^2$  of 305.85 and 301.18 for 250 degrees of freedom, respectively, as shown in figure 6. The pulsed flux obtained with Hitomi accumulated within the time interval of the  $\Delta\phi$  phase is summarized in table 6. Therefore, the  $3\sigma$  upper limit values of enhancement in terms of flux can be obtained by multiplying the values in table 5 (subsection 3.1) by those in table 6. The upper limits of enhancements of MP-GRPs in the X-ray flux in the 2–300 keV band within the phases of 0.20 or 0.03 become  $(24 \text{ or } 3.3) \times 10^{-12} \text{ erg cm}^{-2}$ , respectively, and the same for IP-GRPs were  $(93 \text{ or } 9.9) \times 10^{-12} \text{ erg cm}^{-2}$ , respectively.

## 4 Discussion

With the simultaneous observations of the Crab with Hitomi and the Kashima radio telescope, correlation studies in the X-ray band with about 1000 GRPs have been performed (section 2). No significant changes in the X-ray pulse profiles were detected along all the phase bins at the GRP cycles (section 3), and the  $3\sigma$  upper limit values for the MP- and IP-GRPs in the 2–300 keV band with Hitomi were  $\xi = 22\%$  and  $80\%$  within the time interval of  $\Delta\phi = 0.200$  phase, as summarized in table 5. The upper limits in the

4.5–10 keV and the 70–300 keV bands were obtained for the first time with Hitomi, and those in other bands were consistent with previous works (Bilous et al. 2012; Mikami et al. 2014), as shown in figure 7. Our results constitute the second case of a study in the hard X-ray band where the flux (in  $\nu F_\nu$  space) of the pulsed component of the Crab pulsar became the highest, following a previous report of a marginal detection at the  $2.7\sigma$  level with Suzaku (Mikami et al. 2014). Our results were mainly limited by the photon numbers in the X-ray band, and the statistical errors dominated the results. The pulse shape in the X-ray band was observationally confirmed to be stable with a  $1\sigma$  fluctuation of  $\sim 0.7\%$  level by Rossi X-ray Timing Explorer (RXTE) showing about twice as intensive pulses (Patt et al. 1999; Vivekanand 2001), which could be shallow “giant X-ray pulses” (GXPs) but the timing correlations between these shallow GXPs and the GRPs were unknown. In our X-ray correlation study using the Hitomi satellite, we could not identify such GXPs due to a poor effective area.

As described in subsection 3.1, no significant variabilities were detected in the X-ray pulse profiles of 14 cycles before and after the GRPs. Similarly, in the optical band, the enhancements related to the GRPs only happen in narrow time intervals ( $\sim 100 \mu\text{s}$ ) at the pulse peak, and the pulse profiles in other phases were stable (Shearer et al. 2003). These facts indicate that the magnetosphere is stable during the GRPs, which should originate from a local place within the magnetosphere.

What happens during a GRP on the pulsar, when the structure of the magnetosphere does not change? Here, we assumed the emission mechanism of the optical pulses is synchrotron emission, like X-ray pulses, because the optical emission seems to have the same origin as that of the X-rays from the multiwavelength spectrum of the pulsed component of the pulsar (e.g., see Bühler & Blandford 2014). To increase the synchrotron emission temporarily on a short time scale of  $\mu\text{s}$ , whilst maintaining the structure of the



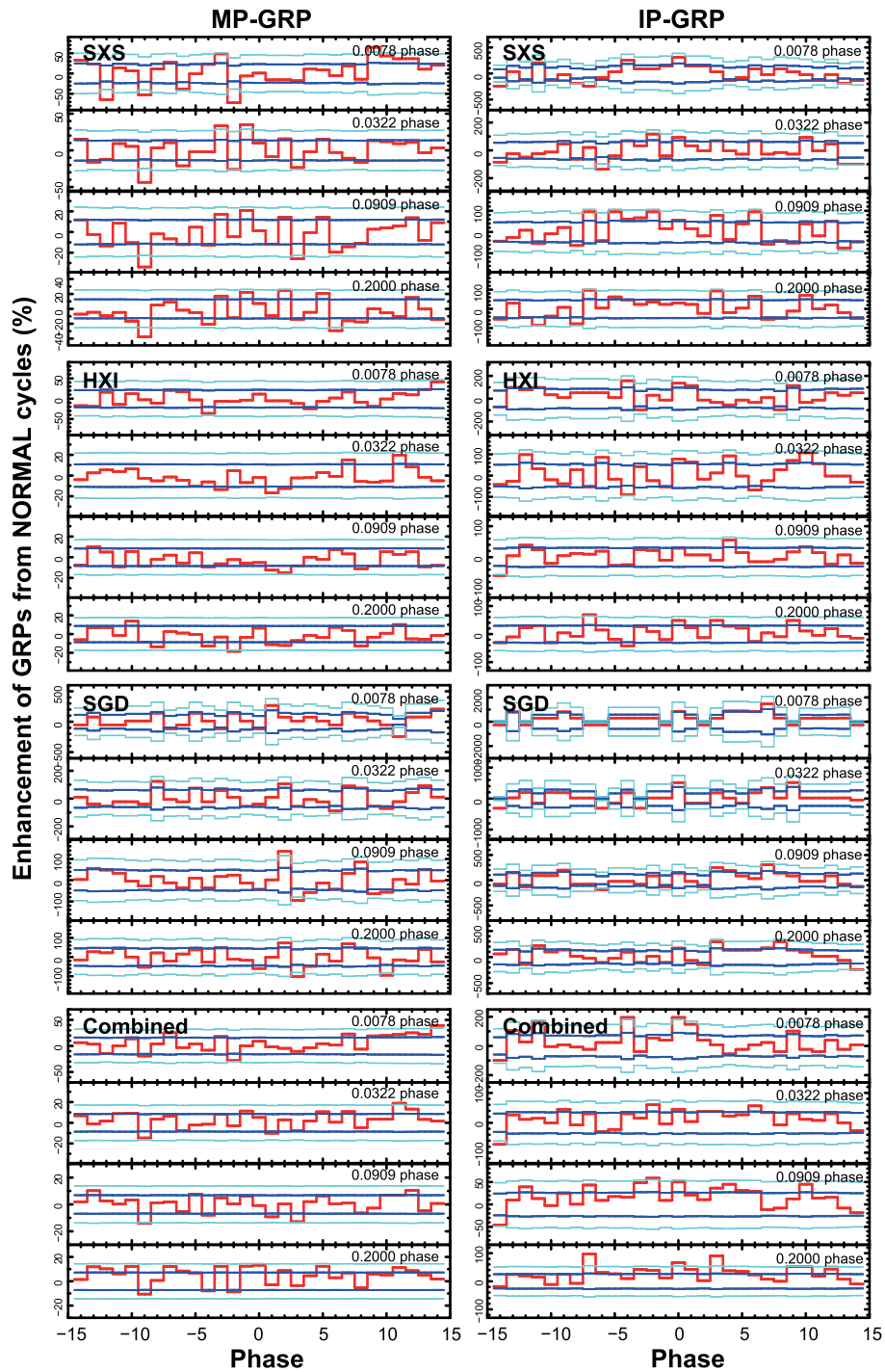


**Fig. 5.** Enhancement of inter-pulse or main pulse on the MP-GRP (left) or IP-GRP (right). From the top to bottom panels, the SXS, HXI, SGD-1, and combined data are shown. The enhancements of GRP relative to normal cycles were measured at the corresponding pulse peaks (i.e., inter-pulse or main pulse) with 0.0078, 0.0322, 0.0909, and 0.200 phase widths, as shown from top to bottom in each plot. The enhancement, as a percentage, is shown in red, and statistical uncertainties of  $1\sigma$  and  $2\sigma$  are shown in blue and green colors, respectively. (Color online)

magnetosphere, only two candidates can be considered: (a) an increase in the number of particles for radiation, or (b) a change in the local magnetic field strength. However, the case (b) would be considered difficult to achieve normally, and the pulse phase need not be aligned to the main pulse

or inter-pulse, and therefore it is straightforward to think that the case (a) is the origin of the optical enhancement at GRPs. Such an occasion might occur after a magnetic reconnection near the light cylinder (Istomin 2004) resulting in a higher-density plasma than the Goldreich-Julian density

**Table 5.** Upper limits of enhancement of GRP ( $3\sigma$ ).

Instrument*	Energy band	MP-GRP	IP-GRP
$\Delta\varphi = 0.2000$ phase			
SXS	2–10 keV	40%	130%
HXI	5–80 keV	30%	90%
SGD-1	10–300 keV	110%	420%
all	2–300 keV	22%	80%
$\Delta\varphi = 0.0322$ phase			
SXS	2–10 keV	90%	180%
HXI	5–80 keV	40%	200%
SGD-1	10–300 keV	200%	1100%
all	2–300 keV	25%	110%

\*Here, “all” represents the sum of the SXS, HXI, and SGD-1 instruments.

in the GRP region (Lyutikov 2007). In the Crab pulsar, the emission regions for radio, optical, and X-rays are normally considered to be close to each other because the pulses are well aligned in these energy bands, although the pulse profile in the X-ray band is wider than that in radio. If the number of particles for synchrotron emission increases in a local region where very short GRPs are emitted, a possible X-ray enhancement should also occur very soon, within about  $10 \mu\text{s}$  just on the pulse peak, like the optical and radio cases. If such a short enhancement were to be detected in the X-ray band, we would be able to reinforce the idea (a), but the fine pulse profiles divided by  $1/128$  phases with Hitomi (figure 3) do not show such enhancements at the peak statistically.

Finally, we discuss the energy balance between the X-ray upper limit of the pulse peak flux ( $\xi$ ) and the radiation energy of the GRP in the radio band,  $E_{\text{radio}}$ . As described in subsection 3.2, the enhancements at the pulse peaks  $\xi$  were within the  $2\sigma$  fluctuation among the 29 cycles around

**Table 6.** Pulsed flux of Crab pulsar.

Instrument	Energy band	$\Delta\varphi$	Main pulse*	Inter pulse*
SXS	2–10 keV	0.20	$31 \pm 5$	$30 \pm 4$
HXI	5–80 keV	0.20	$59^{+9}_{-8}$	$62 \pm 9$
SGD	10–300 keV	0.20	$76^{+11}_{-10}$	$87 \pm 13$
all	2–300 keV	0.20	$108^{+16}_{-15}$	$116 \pm 17$
SXS	2–10 keV	0.03	$4.0 \pm 0.6$	$2.7 \pm 0.4$
HXI	5–80 keV	0.03	$7.0 \pm 1.0$	$5.0 \pm 0.8$
SGD	10–300 keV	0.03	$10 \pm 2$	$6.9 \pm 1.5$
all	2–300 keV	0.03	$13 \pm 2$	$9.0 \pm 1.5$

\*X-ray flux in  $10^{-12} \text{ erg cm}^{-2}$  at the energy band accumulated within the phase width ( $\Delta\varphi$ ).

GRPs, and the upper limit of  $\xi$  in flux was obtained at about  $3.3 \times 10^{-12} \text{ erg cm}^{-2}$  accumulated in the time interval of  $\Delta\varphi = 0.03$  phase. The threshold of detection of GRPs in our radio observation was  $2.2 \text{ kJy } \mu\text{s}$  (sub-subsection 2.2.4), which corresponds to a total emission energy per area of  $E_{\text{radio}} > 2.2 \times 10^{-17} \text{ erg cm}^{-2}$  in a  $10 \mu\text{s}$  accumulation under the assumption that the GRP pulses emit with 1 GHz width in the radio band (Mikami et al. 2016). Interestingly, the optical enhancement of  $\xi_{\text{opt}}(0.003 \text{ phase}) = 3\%$  reported by Shearer et al. (2003) within  $100 \mu\text{s}$  bins corresponds to an energy roughly equivalent to  $E_{\text{radio}}$ . Therefore, we assume here that the radiation energy of the possible X-ray enhancement is almost equivalent to  $E_{\text{radio}}$ , although the pulsed energy spectrum of Crab (e.g., Bühler & Blandford 2014) indicates that the optical light and X-rays have different origins. If an X-ray detection is performed with rather wide phase bins ( $\Delta\varphi = 0.20$  phase around the peak), it appears at  $\xi_X(0.20 \text{ phase}) = 2 \times 10^{-5}\%$  of the X-ray normal pulses in the 2–300 keV band within the same phase bins. This enhancement appears better at  $\xi_X(0.0003 \text{ phase})$

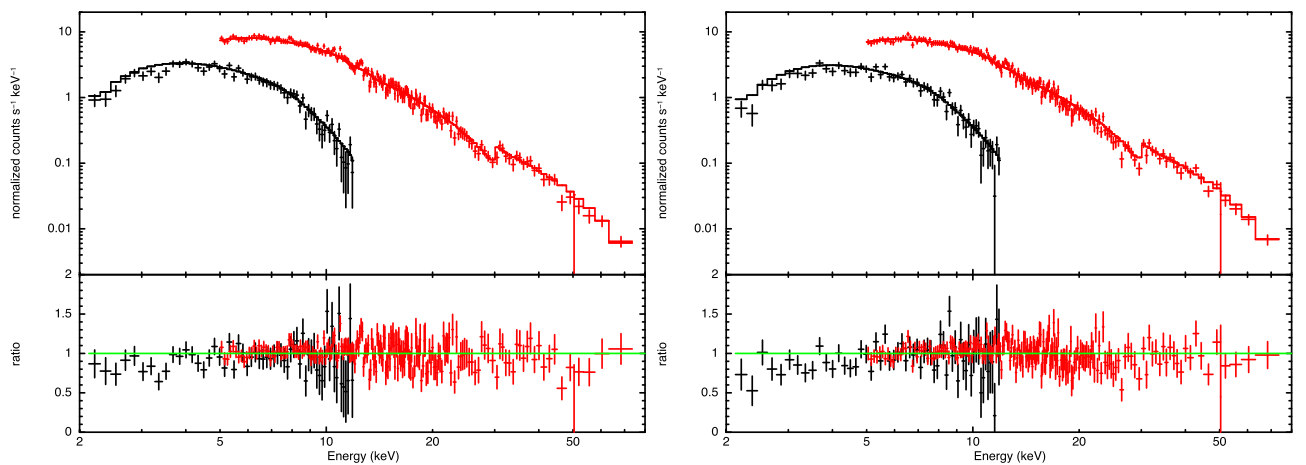


**Fig. 6.** X-ray spectra during the main pulses (left) and inter-pulses (right), respectively. The spectra with the SXS and the HXI are shown in black and red crosses, respectively. The best-fit power-law models are shown in red and black lines for the SXS and HXI, respectively. The lower panels represent the ratio between the data and the model. (Color online)

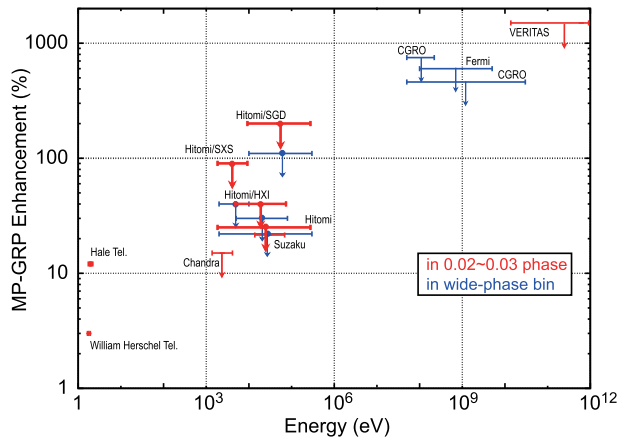


**Fig. 7.** Enhancement of MP-GRPs of the Crab pulsar in various energy bands obtained by the William Herschel Telescope (Shearer et al. 2003), Hale telescope (Strader et al. 2013), Chandra (Bilous et al. 2012), Suzaku (Mikami et al. 2014), Hitomi (this work), CGRO (Lundgren et al. 1995; Ramanamurthy & Thompson 1998), Fermi (Bilous et al. 2011), and VERITAS (Aliu et al. 2012). All the upper limits shown with arrows represent  $3\sigma$  values. The red and blue cases indicate the enhancement measured in a short phase width ( $\Delta\phi = 0.02\text{--}0.03$  phase) and wider phase width ( $\Delta\phi > 0.1$ ), respectively. Note that the thresholds of GRP detections in the radio band were different in each telescope. (Color online)

$= 0.02\%$  of normal pulse flux, when the X-ray observation can resolve the  $10\ \mu\text{s}$  time bin at the pulse peak. But the value is still undetectable under the poor statistics of our Hitomi data and the timing accuracy (Terada et al. 2017). Therefore, the results did not statistically rule out variations correlated with the GRPs, because the possible X-ray enhancement may appear as a  $>0.02\%$  brightening of the pulse peak under such conditions. We can expect future X-ray missions with larger effective area and better timing capability, such as the recently launched NICER mission (Gendreau et al. 2016), to continue the X-ray correlation studies of GRPs. If GXP appears in short phase bins and are correlated with GRPs, NICER may detect the enhancement in the X-ray band, although the sensitivity peak of NICER is at a softer energy band than that of the previous, larger-area mission RXTE, so the count rate expected for Crab pulses is comparable.

## Acknowledgments

We acknowledge the support of the JSPS Core-to-Core Program. We thank all the JAXA members who have contributed to the ASTRO-H (Hitomi) project. All U.S. members gratefully acknowledge support through the NASA Science Mission Directorate. Stanford and SLAC members acknowledge support via DoE contract to SLAC National Accelerator Laboratory DE-AC3-76SF00515. Part of this work was performed under the auspices of the US DoE by LLNL under Contract DE-AC52-07NA27344. Support from the European Space Agency is gratefully acknowledged. French members acknowledge support from CNES, the Centre National d'Études Spatiales. SRON is supported by NWO, the Netherlands

Organization for Scientific Research. The Swiss team acknowledges the support of the Swiss Secretariat for Education, Research and Innovation (SERI). The Canadian Space Agency is acknowledged for the support of the Canadian members. We acknowledge support from JSPS/MEXT KAKENHI grant numbers 15H00773, 15H00785, 15H02090, 15H03639, 15K05088, 15K05069, 15H05438, 15K05107, 15K17610, 15K17657, 16J02333, 16J06773, 16H00949, 16H06342, 16K05295, 16K05296, 16K05300, 16K13787, 16K17672, 16K17673, 17H02864, 17K05393, 21659292, 23340055, 23340071, 23540280, 24105007, 24540232, 25105516, 25109004, 25247028, 25287042, 25400236, 25800119, 26109506, 26220703, 26400228, 26610047, 26800102, JP15H02070, JP15H03641, JP15H03642, JP15H06896, JP16H03983, JP16K05296, JP16K05309, and JP16K17667. The following NASA grants are acknowledged: NNX15AC76G, NNX15AE16G, NNX15AK71G, NNX15AU54G, NNX15AW94G, and NNG15PP48P to Eureka Scientific. This work was partly supported by Leading Initiative for Excellent Young Researchers, MEXT, Japan, and also by the Research Fellowship of JSPS for Young Scientists. H. Akamatsu acknowledges the support of NWO via a Veni grant. C. Done acknowledges STFC funding under grant ST/L00075X/1. A. Fabian and C. Pinto acknowledge ERC Advanced Grant 340442. P. Gandhi acknowledges a JAXA International Top Young Fellowship and UK Science and Technology Funding Council (STFC) grant ST/J003697/2. Y. Ichinohe, K. Nobukawa, and H. Seta are supported by the Research Fellow of JSPS for Young Scientists program. N. Kawai is supported by the Grant-in-Aid for Scientific Research on Innovative Areas “New Developments in Astrophysics Through Multi-Messenger Observations of Gravitational Wave Sources.” S. Kitamoto is partially supported by the MEXT Supported Program for the Strategic Research Foundation at Private Universities, 2014–2018. B. McNamara and S. Safi-Harb acknowledge support from NSERC. T. Dotani, T. Takahashi, T. Tamagawa, M. Tsujimoto, and Y. Uchiyama acknowledge support from the Grant-in-Aid for Scientific Research on Innovative Areas “Nuclear Matter in Neutron Stars Investigated by Experiments and Astronomical Observations.” N. Werner is supported by the Lendület LP2016-11 grant from the Hungarian Academy of Sciences. D. Wilkins is supported by NASA through Einstein Fellowship grant number PF6-170160, awarded by the Chandra X-ray Center and operated by the Smithsonian Astrophysical Observatory for NASA under contract NAS8-03060.

We thank contributions by many companies, including in particular NEC, Mitsubishi Heavy Industries, Sumitomo Heavy Industries, and Japan Aviation Electronics Industry. Finally, we acknowledge strong support from the following engineers. JAXA/ISAS: Chris Baluta, Nobutaka Bando, Atsushi Harayama, Kazuyuki Hirose, Kosei Ishimura, Naoko Iwata, Taro Kawano, Shigeo Kawasaki, Kenji Minesugi, Chikara Natsukari, Hiroyuki Ogawa, Mina Ogawa, Masayuki Ohta, Tsuyoshi Okazaki, Shin-ichiro Sakai, Yasuko Shibano, Maki Shida, Takanobu Shimada, Atsushi Wada, and Takahiro Yamada; JAXA/TKSC: Atsushi Okamoto, Yoichi Sato, Keisuke Shinozaki, and Hiroyuki Sugita; Chubu University: Yoshiharu Namba; Ehime University: Keiji Ogi; Kochi University of Technology: Tatsuro Kosaka; Miyazaki University: Yusuke Nishioka; Nagoya University: Housei Nagano; NASA/GSFC: Thomas Bialas, Kevin Boyce, Edgar Canavan, Michael DiPirro, Mark Kimball, Candace Masters, Daniel McGuinness, Joseph Miko, Theodore Muench, James Pontius, Peter Shirron, Cynthia Simmons, Gary Sneiderman, and Tomomi Watanabe; ADNET Systems: Michael Witthoef, Kristin Rutkowski, Robert S. Hill, and Joseph Eggen; Wyle

Information Systems: Andrew Sargent and Michael Dutka; Noqi Aerospace Ltd: John Doty; Stanford University/KIPAC: Makoto Asai and Kirk Gilmore; ESA (Netherlands): Chris Jewell; SRON: Daniel Haas, Martin Frericks, Philippe Laubert, and Paul Lowes; University of Geneva: Philipp Azzarello; CSA: Alex Koujelev and Franco Moroso.

## Author contributions

Y. Terada led this study in data analysis and writing drafts, in addition to the Hitomi timing calibration and software preparation. X-ray data analyses and calibrations were done with T. Enoto, S. Koyama, A. Bamba S. Nakashima, T. Yaqoob, H. Takahashi, S. Watanabe, and K. Oshimizu. T. Terasawa led the radio data analysis with M. Sekido, K. Takehiji, E. Kawai, H. Misawa, F. Tsuchiya, R. Yamazaki, E. Kobayashi, S. Kisaka, and T. Aoki. T. Dotani, L. Gallo, R. Mushotzky, C. Ferrigno, K. Pottschmidt, M. Loewenstein, M. Tsujimoto, S. Safi-Harb, and P. Kretschmar improved the draft.

## Appendix 1. Details of radio data reduction

### A.1.1 TEMPO2 timing package

The pulsar timing package TEMPO2 (Hobbs et al. 2006) gives the function  $\tilde{f}(t_{\text{UTC}})$  to convert the observation time in UTC,  $t_{\text{UTC}}$ , to the time at the Solar System barycenter [TDB],  $\tilde{t}_{\text{TDB}}$ . TEMPO2 also gives the signal frequency  $\nu_{\text{ISM}}$  in the rest frame of the interstellar matter (ISM) corresponding to the observation frequency  $\nu_{\text{obs}}$ , which is Doppler shifted by the revolutionary and rotationary motion of the Earth with respect to the Solar System barycenter. We define the Doppler factor  $\eta \equiv \nu_{\text{obs}}/\nu_{\text{ISM}}$ .

### A.1.2. Calculations of $S/N$

We dedispersed the raw antenna voltage data of the channel  $k$ ,  $V_k^{\text{raw}}(t)$ , to obtain  $V_k(t)$ . We integrated  $|V_k(t)|^2$  over the time interval of  $\Delta t = 10 \mu\text{s}$ ,

$$\mathcal{E}_k(t_n) = \frac{1}{\Delta t} \int_{t_n}^{t_{n+1}} |V_k(t')|^2 dt', \quad (\text{A1})$$

where we defined the binned times as  $t_n = t_{\text{start}} + n\Delta t$  (here we represent  $t$  and  $t_n$  by UTC;  $t_{\text{start}} = 12:15:00$  UT). Between channels  $k$  and 6, there is an arrival time difference owing to the propagation group delay,

$$\tau_{k,6} = \frac{e^2}{2\pi m_e c} DM \left\{ \frac{1}{\nu_k^2} - \frac{1}{\nu_6^2} \right\} \eta, \quad (\text{A2})$$

where  $(e, m_e, c)$  are usual physical quantities,  $DM$  the dispersion measure, and  $\nu_k$  and  $\nu_6$  the highest frequencies of

bands  $k$  and 6. The Doppler factor  $\eta$  appears in equation (A2) since  $\tau_{k,6}$ ,  $\nu_k$ , and  $\nu_6$  are defined in the observer's frame. We combined incoherently  $\mathcal{E}_0(t_n)$ ,  $\mathcal{E}_1(t_n)$ , ...,  $\mathcal{E}_6(t_n)$  as

$$\mathcal{E}_{\text{sum}}(t_n) = \sum_{k=0,1,4,5,6} \mathcal{E}_k(t_n - \tau_{k,6}), \quad (\text{A3})$$

where appropriate interpolations were taken to calculate the right-hand side of equation (A3).

We calculated the average  $\bar{\mathcal{E}}_{\text{sum}}$  and standard deviation  $\sigma_{\text{sum}}$  of  $\mathcal{E}_{\text{sum}}(t_n)$  over an appropriate longer time interval ( $\Delta T$ , for which we take 1 s). Ideally,  $\bar{\mathcal{E}}_{\text{sum}}$  and  $\sigma_{\text{sum}}$  are constant in time. In reality, however, they showed slight and gradual variations in time  $T_M (= t_{\text{start}} + M\Delta T, M = 0, 1, 2, \dots)$ . We calculate the  $S/N$  at  $t_n$  for  $T_M \leq t_n < T_{M+1}$  as

$$\mathcal{S}_{\text{sum}}(t_n) = \frac{1}{\sigma_{\text{sum}}(T_M)} [\mathcal{E}_{\text{sum}}(t_n) - \bar{\mathcal{E}}_{\text{sum}}(T_M)]. \quad (\text{A4})$$

With a given threshold  $\mathcal{S}_{\text{sum,thr}}$ , we selected ‘‘GRP candidates’’ for each one in which there was an enhancement,<sup>3</sup>  $\mathcal{S}_{\text{sum}}(t_n) \geq \mathcal{S}_{\text{sum,thr}}$ .

### A.1.3. Time-domain RFI rejection

To eliminate RFI further, we conducted the following auxiliary process. We calculated the squared antenna voltages  $\mathcal{E}_k^{\text{raw}}(t_n)$  following equation (A1), except that we used  $V_k^{\text{raw}}(t)$  instead of  $V_k(t)$ . From  $\mathcal{E}_k^{\text{raw}}(t_n)$  we then calculated

$$\mathcal{E}_{\text{sum}}^{\text{raw}}(t_n) \equiv \sum_{k=0,1,4,5,6} \mathcal{E}_k^{\text{raw}}(t_n), \quad (\text{A5})$$

and their average and standard deviation,  $\bar{\mathcal{E}}_{\text{sum}}^{\text{raw}}(T_M)$  and  $\sigma_{\text{sum}}^{\text{raw}}(T_M)$ . We watched the behaviors of  $\sigma_{\text{sum}}(T_M)$  and  $\sigma_{\text{sum}}^{\text{raw}}(T_M)$  throughout the observation interval. When  $\sigma_{\text{sum}}(T_M) < \sigma_{\text{sum}}^{\text{raw}}(T_M)$ , we reject the data  $\mathcal{S}_{\text{sum}}(t_n)$  for  $T_M \leq t_n < T_{M+1}$  as being affected by RFI.

### A.1.4. Rotation phase and GRP identification

We calculated the phase  $\varphi_n$  of a GRP candidate at the time in UTC  $t_n$ ,

$$\varphi_n = \text{frac}(y) \quad \text{with} \quad y = y_0 + \nu_{\text{rot}} \tilde{t}_n + 0.5 \dot{\nu}_{\text{rot}} \tilde{t}_n^2, \quad (\text{A6})$$

where  $\tilde{t}_n = \tilde{f}(t_n)$  is the time in TDB,  $\text{frac}(y)$  is the fractional part of  $y$ ,  $y_0$  is the initial phase at 00:00:00 TDB, and  $\nu_{\text{rot}}$  and  $\dot{\nu}_{\text{rot}}$  are the rotation frequency and its time derivative from the Jodrell Bank monthly ephemeris (table 2). In the operation of equation (A6), we also recorded the

<sup>2</sup> We use the term ‘‘integrate’’ for simplicity. In reality, of course, we calculated equation (A1) as finite sums over  $t_n \leq t < t_{n+1}$  with an original sampling time step  $\delta t = 15.625$  ns.

<sup>3</sup> A strong GRP gives enhancements of the average and standard deviation, so that the  $S/N$  obtained by equation (A4) is reduced. To avoid this effect, we replace the average and standard deviation in equation (A4) with the values interpolated from those obtained in the surrounding time intervals that are unaffected by GRPs.



integer part of  $y$  as the sequential pulse number of the day,  $N_{\text{pulse}}$ , which is to be used for the GRP and X-ray photon comparison.

As discussed in sub-subsection 2.2.4, we classify the GRP candidates according to their values of  $\varphi$  by setting two selection ranges,  $(\varphi_{\text{MP},1}, \varphi_{\text{MP},2})$  for main pulse GRPs, and  $(\varphi_{\text{IP},1}, \varphi_{\text{IP},2})$  for inter-pulse GRPs. With the choice of  $\Delta t = 10 \mu\text{s}$ , two thirds of GRP candidates in the 1.4–1.7 GHz band are isolated in  $\varphi$  space. However, for the remaining one third of (stronger) GRPs, 2–4 GRP candidates of the same  $N_{\text{pulse}}$  are found in the same selection range for  $\varphi$ . For such cases, we count them as one GRP, either main pulse or inter-pulse.

For a GRP occurring near the binned time boundary  $t = t_n$ , its contribution is divided into  $\mathcal{E}_{\text{sum}}(t_n)$  and  $\mathcal{E}_{\text{sum}}(t_{n+1})$ , and the corresponding  $\mathcal{S}_{\text{sum}}(t_n)$  and  $\mathcal{S}_{\text{sum}}(t_{n+1})$  are artificially lowered (sometimes both are less than  $\mathcal{S}_{\text{sum,thr}}$ ). To avoid miscounting of GRPs caused by this effect, we repeated the procedure from equation (A1) to equation (A4) for the binned time with a shift of  $\Delta t/2$ . First we calculate

$$\mathcal{E}_k(t_{n+\frac{1}{2}}) = \frac{1}{\Delta t} \int_{t_n+\frac{\Delta t}{2}}^{t_{n+1}+\frac{\Delta t}{2}} |V_k(t')|^2 dt'. \quad (\text{A1}')$$

If the resultant  $\mathcal{S}_{\text{sum}}(t_{n+\frac{1}{2}})$  exceeds  $\mathcal{S}_{\text{sum,thr}}$ , this GRP is “rescued from the sea of the noise.” We found that about 10% of GRPs are thus rescued.

### A.1.5. Radiometer equation

The flux density  $\mathcal{F}$  is calculated as  $C \times (S/N)$ , with  $C$  given by the radiometer equation (Dicke 1946; Lorimer & Kramer 2004)

$$C = \frac{\text{SEFD} + S_{\text{CN}}}{\sqrt{\Delta \nu_{\text{sum}} \Delta t}} [\text{Jy}], \quad (\text{A7})$$

where SEFD is the system equivalent flux density, and  $S_{\text{CN}}$  is the flux density of the Crab nebula. With the representative values  $\text{SEFD} = 500 \text{ Jy}$  and  $S_{\text{CN}} = 810 \text{ Jy}$  (Mikami et al. 2016), we get  $C = 40.2 \text{ Jy}$  for  $\Delta \nu_{\text{sum}} = 106.36 \text{ MHz}$  (sub-subsection 2.2.3) and  $\Delta t = 10 \mu\text{s}$ . The GRP threshold  $S/N = 5.5$  used in subsection 2.2 corresponds to a flux density threshold of  $\mathcal{F} = 220 \text{ Jy}$ , or a pulse energy threshold  $\mathcal{F} \Delta t = 2.2 \text{ kJy } \mu\text{s}$ .

## Appendix 2. Extraction of the SGD photo-absorption mode

On the timing analyses of the SGD-1 data in subsection 2.3, the photo-absorption events were extracted from the unscreened event files to have more effective areas than

those of the standard Compton scattered events: the expression

```
FLAG_LCHKMIO == b0 && FLAG_CCBUSY[1] == b0
&& FLAG_CCBUSY[2] == b0 && FLAG_CCBUSY[3]
== b0 && FLAG_HITPAT[1] == b0 &&
FLAG_HITPAT[2] == b0 && FLAG_HITPAT[3]
== b0 && FLAG_HITPAT[4] == b0 &&
FLAG_FASTBGO[1] == b0 && FLAG_FASTBGO[2]
== b0 && FLAG_FASTBGO[3] == b0 &&
FLAG_FASTBGO[4] == b0 && FLAG_SEU == b0
&& FLAG_LCHK == b0 && FLAG_CALMODE == b0
&& FLAG_TRIGPAT[29] == b0 && CATEGORY ==
85 && MATTYPE == 1 && NUMSIGNAL == 1
```

was applied to the UFA event, and standard GTI in the second extension of the cleaned events were also applied.

## References

- Aliu, E., et al. 2012, *ApJ*, 760, 136
- Angelini, L., et al. 2017, *J. Astron. Telesc. Instrum. Syst.*, 4, 011207
- Bilous, A. V., Kondratiev, V. I., McLaughlin, M. A., Ransom, S. M., Lyutikov, M., Mickaliger, M., & Langston, G. I. 2011, *ApJ*, 728, 110
- Bilous, A. V., McLaughlin, M. A., Kondratiev, V. I., & Ransom, S. M. 2012, *ApJ*, 749, 24
- Bühler, R., & Blandford, R. 2014, *Rep. Prog. Phys.*, 77, 066901
- Burke-Spolaor, S., et al. 2012, *MNRAS*, 423, 1351
- Chatterjee, S., et al. 2017, *Nature*, 541, 58
- Cordes, J. M., & Wasserman, I. 2016, *MNRAS*, 457, 232
- DeLaunay, J. J., et al. 2016, *ApJ*, 832, L1
- Dicke, R. H. 1946, *Radio Sci.*, 17, 268
- Gendreau, K. C., et al. 2016, *SPIE Proc.*, 9905, 99051H
- Hankins, T. H., Kern, J. S., Weatherall, J. C., & Eilek, J. A. 2003, *Nature*, 422, 141
- Hankins, T. H., & Rickett, B. J. 1975, in *Methods in Computational Physics*, Vol. 14: Radio Astronomy (New York: Academic Press, Inc.), 55
- Hitomi Collaboration 2016, *Nature*, 535, 117
- Hobbs, G. B., Edwards, R. T., & Manchester, R. N. 2006, *MNRAS*, 369, 655
- Istomin, Y. N. 2004, in *IAU Symp. 218, Young Neutron Stars and Their Environments*, ed. F. Camilo & B. M. Gaensler (San Francisco: ASP), 369
- Kelley, R. L., et al. 2018, *J. Astron. Telesc. Instrum. Syst.*, submitted
- Knight, H. S. 2006, *Chin. J. Astron. Astrophys. Suppl.*, 6, 41
- Kuzmin, A., Losovsky, B. Ya., Jordan, C. A., & Smith, F. G. 2008, *A&A*, 483, 13
- Lorimer, D. R., Bailes, M., McLaughlin, M. A., Narkevic, D. J., & Crawford, F. 2007, *Science*, 318, 777
- Lorimer, D. R., & Kramer, M. 2004, *Handbook of Pulsar Astronomy* (Cambridge: Cambridge University Press)
- Lundgren, S. C., Cordes, J. M., Ulmer, M., Matz, S. M., Lomatch, S., Foster, R. S., & Hankins, T. 1995, *ApJ*, 453, 433
- Lyne, A. G., Pritchard, R. S., & Graham-Smith, F. 1993, *MNRAS*, 265, 1003
- Lyutikov, M. 2007, *MNRAS*, 381, 1190



- Majid, W. A., Naudet, C. J., Lowe, S. T., & Kuiper, T. B. H. 2011, *ApJ*, 741, 53
- Mikami, R., et al. 2014, *JPS Conf. Proc.*, 1, 015106
- Mikami, R., et al. 2016, *ApJ*, 832, 212
- Nakajima, H., et al. 2018, *PASJ*, 70, 21
- Nakazawa, K., et al. 2018, *J. Astron. Telesc. Instrum. Syst.*, submitted
- Patt, B. L., Ulmer, M. P., Zhang, W., Cordes, J. M., & Arzoumanian, Z. 1999, *ApJ*, 522, 440
- Popov, M. V., & Stappers, B. 2007, *A&A*, 470, 1003
- Ramanamurthy, P. V., & Thompson, D. J. 1998, *ApJ*, 496, 863
- Sallmen, S., Backer, D. C., Hankins, T. H., Moffett, D., & Lundgren, S. 1999, *ApJ*, 517, 460
- Shearer, A., Stappers, B., O'Connor, P., Golden, A., Strom, R., Redfern, M., & Ryan, O. 2003, *Science*, 301, 493
- Staelin, D. H., & Reifenstein, E. C., III 1968, *Science*, 162, 1481
- Strader, M. J., et al. 2013, *ApJ*, 779, L12
- Tajima, H., et al. 2018, *J. Astron. Telesc. Instrum. Syst.*, submitted
- Takahashi, T., et al. 2018, *J. Astron. Telesc. Instrum. Syst.*, submitted
- Takefuji, K., et al. 2016, *PASP*, 128, 084502
- Takefuji, K., Takeuchi, H., Tsutsumi, M., & Koyama, Y. 2010, in *Int. VLBI Service for Geodesy and Astrometry 2010 General Meeting Proc., VLBI2010: From Vision to Reality*, NASA/CP 2010-215864, ed. D. Behrend & K. D. Baver (Greenbelt: NASA Goddard Space Flight Center), 378
- Tanaka, T., et al. 2018, *J. Astron. Telesc. Instrum. Syst.*, submitted
- Terada, Y., et al. 2008, *PASJ*, 60, S25
- Terada, Y., et al. 2018, *J. Astron. Telesc. Instrum. Syst.*, 4, 011206
- Thornton, D., et al. 2013, *Science*, 341, 53
- Vivekanand, M. 2001, *A&A*, 373, 236
- Yamasaki, S., Totani, T., & Kawanaka, N. 2016, *MNRAS*, 460, 2875